Vector-based synthesis of finite aperiodic subwavelength diffractive optical elements

Dennis W. Prather and Joseph N. Mait

U.S. Army Research Laboratory, 2800 Powder Mill Road, Adelphi, Maryland 20783

Mark S. Mirotznik

Department of Electrical Engineering, The Catholic University of America, Washington, D.C. 20064

James P. Collins

U.S. Army Research Laboratory, 2800 Powder Mill Road, Adelphi, Maryland 20783

Received August 5, 1997; revised manuscript received December 11, 1997; accepted January 14, 1998

We present an optimization-based synthesis algorithm for the design of diffractive optical elements (DOE's) that are finite in extent, have subwavelength features, and are aperiodic. The subwavelength nature of the DOE's precludes the use of scalar diffraction theory, and their finite extent and aperiodic nature prevents the use of coupled-wave analysis. To overcome these limitations, we apply the boundary element method (BEM) as the propagation model in the synthesis algorithm. However, the computational costs associated with the conventional implementation of the BEM prevent the design of realistic DOE's in reasonable time frames. Consequently, an alternative formulation of the BEM that exploits DOE symmetry is developed and implemented on a parallel computer. Designs of finite extent, subwavelength, and aperiodic DOE's, such as a lens and a focusing beam splitter, are presented. © 1998 Optical Society of America [S0740-3232(98)00306-8]

OCIS codes: 0.50.1970, 050.1940, 050.1960.

1. INTRODUCTION

Diffractive optical elements (DOE's) that have feature sizes smaller than the wavelength of illumination are referred to as subwavelength diffractive optical elements (SWDOE's). Like their superwavelength counterparts, binary SWDOE's are the simplest to fabricate. However, unlike their superwavelength counterparts, researchers have shown that binary SWDOE's can achieve diffraction efficiencies in excess of 90%. Unfortunately, the application of such elements is limited not only by fabrication technology but also by the availability of the tools required for their analysis and design.

Considerable effort has been extended over the past 15 years on the analysis of infinitely periodic elements, specifically, gratings, that have subwavelength features.[1] More recently, designs for subwavelength gratings have begun to appear in the literature.[2–7]

By comparison, little work has appeared on the analysis of finite, aperiodic elements and even less on their design. We have shown recently that the boundary element method (BEM) is an effective tool for the vector-based analysis of diffraction from finite, aperiodic SWDOE's.[8] In this paper we extend our work to include the optimal design of such elements.

We begin in Section 2 with an overview of our synthesis algorithm, which includes a discussion of the determination of the initial input, the BEM used to model diffraction, and the optimization routines we used in our design. In Section 3 we present the results of our algorithm as applied to the design of a subwavelength lens and a 1-to-2 fan-out element. We summarize our contributions and provide concluding remarks in Section 4.

2. SYNTHESIS ALGORITHM FOR SUBWAVELENGTH DIFFRACTIVE OPTICAL ELEMENT DESIGN

Although some SWDOE's can be designed with analytical techniques,[2,9] in general, most cannot. For these latter SWDOE's, one uses a synthesis algorithm to determine their optimal profile by casting the problem of design into one of optimization.[10] As illustrated in Fig. 1, the synthesis algorithm models the forward propagation of an initial candidate profile to an observation plane where its performance is evaluated. Although both forward and inverse propagation models can be used in synthesis algorithms, e.g., for scalar-based designs of DOEs,[10] generally speaking, vector-based diffraction models are difficult to invert, which dictates their use for forward propagation only. Once it is evaluated, DOE performance is used by the optimization routine to determine changes in the candidate profile. This process is repeated until either the performance of the DOE satisfies design criteria or the algorithm converges.

In our synthesis algorithm the BEM[8] is used as the forward propagation model, and both simulated annealing (SA) and a rapid-annealing routine, referred to as simulated quenching (SQ), are used for optimization. Although the BEM represents an efficient diffraction model for the analysis of DOE's, to allow for the design of real-

0740-3232/98/061599-09$15.00

istic SWDOE's within reasonable time frames we developed a more efficient formulation of the BEM that exploits DOE symmetry, and we implemented it on a parallel computer. We refer to this formulation of the BEM as the semi-infinite and symmetric BEM (SSBEM).

In this section we discuss each step of the synthesis algorithm illustrated in Fig. 1. We begin with our technique for determining the initial finite, aperiodic SWDOE that is input into the algorithm.

A. Determination of Initial Input

Computational costs of a design can be contained if a good initial guess, as opposed to a completely random one, is input into the algorithm. To achieve this good initial guess for finite, aperiodic SWDOE's, we generalize the design approach presented by Farn for infinitely periodic gratings.[2] In Farn's approach the binary profile of a subwavelength grating is represented as a Fourier series expansion with unknown coefficients that are functions of the profile transitions. The desired continuous profile is represented by a Fourier series expansion with known coefficients. The transition points can be determined by equating the two expansions. In general this system of equations is difficult to solve; however, Farn found an approximate solution for a linear blazed grating[2]:

$$\alpha_i = iW/(N+1), \tag{1a}$$

$$\beta_i = iW/N, \tag{1b}$$

where, as shown in Fig. 2, α_i and β_i are the start and stop transition points for the ith feature and W is the grating period. The number of features N is determined by dividing the grating period into subperiods of width Δ:

$$N = W/\Delta. \tag{2}$$

We refer to $\Delta = \lambda/2n$ as the subwavelength parameter, where n is the index of refraction for the DOE material. Application of this technique to the design of subwavelength gratings has produced binary devices whose performance, in terms of diffraction efficiency, approaches that of multilevel elements.[2–4]

We extend Farn's technique to include the design of finite, aperiodic SWDOE's by first approximating a continuous-phase profile with a piecewise-linear phase as represented in Figs. 3(a) and 3(b). We then encode the individual linear segments as subwavelength structures with Eqs. (1) and (2). Application of this technique yields a binary profile $f(x)$:

$$f(x) = \sum_{k=1}^{M} \sum_{i=1}^{N_k} \operatorname{rect}\left[\frac{x - (\alpha_{k,i} + \beta_{k,i})/2 - (i-1)\Delta - \sum_{j=1}^{k-1} W_j}{\beta_{k,i} - \alpha_{k,i}}\right], \tag{3}$$

where $\alpha_{k,i}$ and $\beta_{k,i}$ are the start and stop transition points for the ith feature in the kth zone, respectively, and N_k and W_k are the number of subperiods and width of the kth zone, respectively. Application of this technique to Fig. 3(b) yields the binary profile represented in Fig. 3(c).

One way to measure the effectiveness of our design technique is to determine the effective permittivity of the shape function. To determine the effective permittivity of a subwavelength grating, one can use the zeroth-order effective medium theory.[11,12] However, the structures of interest to us are aperiodic and therefore have a spatially varying permittivity. To account for this, we apply the effective medium theory over a small subwavelength region.[13] This produces a local averaging that we model as a convolution[14];

$$\epsilon_{\mathrm{eff,TE}}(x) = \left\{\epsilon_s f(x) + \epsilon_o\left[\operatorname{rect}\left(\frac{x}{D}\right) - f(x)\right]\right\} * \frac{1}{\Delta}\operatorname{rect}\left(\frac{x}{\Delta}\right), \tag{4a}$$

$$\epsilon^{-1}_{\mathrm{eff,TM}}(x) = \left\{\epsilon_s^{-1} f(x) + \epsilon_o^{-1}\left[\operatorname{rect}\left(\frac{x}{D}\right) - f(x)\right]\right\} * \frac{1}{\Delta}\operatorname{rect}\left(\frac{x}{\Delta}\right), \tag{4b}$$

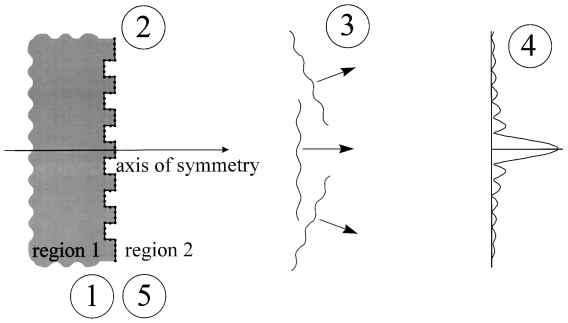

Fig. 1. Diagram of SSBEM-based synthesis algorithm: 1, initial profile; 2, use SSBEM to determine symmetric fields on boundary surface; 3, propagate fields; 4, evaluate performance; 5, modify profile and return to step 2.

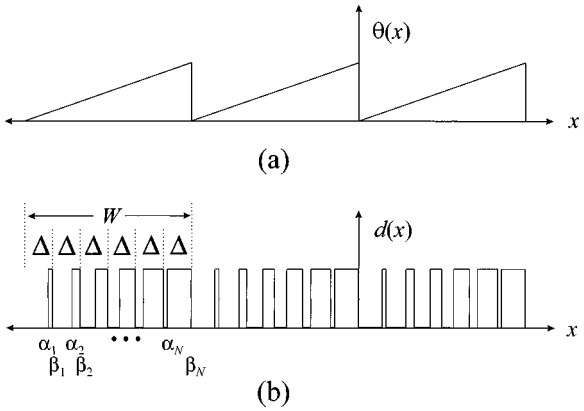

Fig. 2. Subwavelength design of linear blazed grating using Farn's technique: (a) continuous-phase linear blazed grating, (b) binary subwavelength grating.

where D is the SWDOE aperture and $*$ denotes a one-dimensional convolution. Although we are still investigating the validity of this model, application of Eq. (4a) for TE polarization to the structure represented in Fig. 3(c) yields a permittivity that corresponds to the spatially varying index of refraction represented in Fig. 3(d). Except for quantization of the profile that results from the finite extent of the subwavelength features, Fig. 3(d) is a good approximation to Fig. 3(b).

Although the performance of the profiles produced by our technique compares well with that of multilevel devices, because of small feature sizes and large aspect ratios (ratio of minimum feature height to width), they are difficult to fabricate. To overcome this limitation, we enforce fabrication constraints by spatially quantizing the subwavelength profile to a grid that can be fabricated. The lattice spacing of the grid corresponds to the minimum feature $\delta_{\min}$ that can be fabricated [see Fig. 4(a)]. Similarly, we constrain the aspect ratio by scaling the height of the subwavelength profile, as shown in Fig. 4(b). However, this reduces the maximum phase ϕ that the subwavelength profile can impart on the incident field to $\phi = 2\pi\kappa$, where κ is a scale factor between 0 and 1.

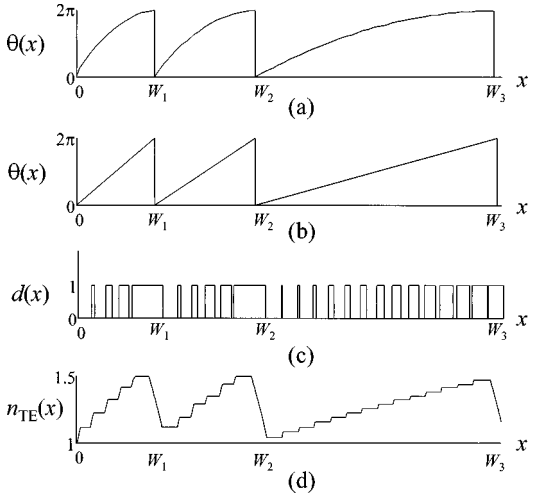

Fig. 3. Subwavelength design of arbitrary phase functions using extension to Farn's technique: (a) continuous-phase function and (b) its piecewise-linear approximation, (c) binary subwavelength diffractive element and (d) its corresponding effective refractive index.

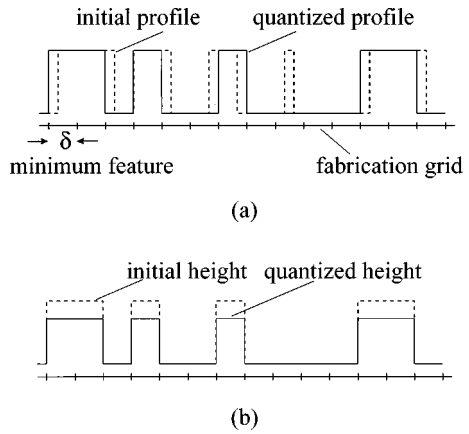

Fig. 4. Application of fabrication constraints to SWDOEs: (a) spatial and (b) depth quantization of binary subwavelength profile.

By enforcing the fabrication constraints in the design of SWDOE's, one ensures that the designed subwavelength profile can be fabricated. However, their performance is degraded from the unconstrained SWDOE. Although this degradation can be significant, as we show, this loss can be recovered and surpassed if the resulting profile is used as the initial input in our synthesis algorithm. In the Subsection 2.B we discuss the BEM as the vector-based forward propagation model, indicated as steps 2 and 3 in Fig. 1.

B. Boundary Element Method

The diffraction model in a synthesis algorithm analyzes the behavior of candidate DOE profiles. The validity of the diffraction model affects the accuracy with which the performance of candidate profiles can be evaluated and thereby limits the efficacy of the synthesis algorithm. Because the DOE's considered in this work contain subwavelength features and are finite in extent and aperiodic, neither scalar theory[10] nor coupled-wave analysis,[1] two commonly used methods for DOE analysis, represents a valid diffraction model. Scalar theory is invalid because of the subwavelength size of the diffractive features, and coupled-wave analysis assumes a grating structure.

As we have shown in our previous work,[8,15] the BEM is a valid diffraction model for the analysis of finite aperiodic SWDOE's and is therefore the forward propagation model that we use for synthesis. However, the traditional formulation of the BEM assumes that the DOE is represented by a sampled version of its (closed) surface boundary. The accurate representation of a realistic DOE therefore requires excessive memory, and the analysis of the DOE requires significant computational effort. As a consequence, application of a traditional closed-boundary BEM to the synthesis of realistic DOE's is prohibitive in terms of computational costs.

To make analysis and synthesis of DOE's more computationally efficient, we modified the BEM by accounting for geometrical properties of the DOE that help reduce computational and memory requirements. For example, if the back side of the substrate on which the DOE is fabricated is planar, it is unnecessary to include it in the analysis. Instead, the diffractive effects of the back side can be accounted for by scaling the amplitude of the incident field by the Fresnel reflection coefficient of the planar dielectric interface.[13]

With the back surface removed, it stands to reason that the semi-infinite BEM should not accurately account for multiple reflections that exist between the front and back surfaces of the DOE. However, we have found that the fields predicted by a semi-infinite BEM analysis agree to within a small percentage with those predicted by a closed-boundary BEM analysis for different substrate thicknesses.[13] One possible explanation for this is that, because the incident beam is finite in extent, the beams reflected back into the DOE are also finite but primarily off axis. Thus, from a geometric perspective, the region over which the incident and the reflected beams interact is negligible.

As indicated in Fig. 5 the once closed boundary is now represented by a segment of finite length; however, unless the incident field is windowed on the front surface of the DOE, errors in the analysis will be produced.[16] This semi-infinite formulation reduces the number of nodes N in the traditional formulation by approximately a factor of two and, because the size of the system of equations is proportional to N^2, reduces four-fold the computational effort and memory requirements.

To analyze the diffraction from the DOE, we assume that the incident field is a uniform TE-polarized plane wave, in which case only the transverse component of the electric field needs to be considered. The solution space is divided into two homogeneous regions: region 1, which contains the DOE, and region 2, which is free space. Derivation of the boundary integral equations that describe the coupling between the fields on the surface of the DOE and those in free space is contained in Appendix A. The key equations are presented here:

$$0 = \mathbf{E}^{\mathrm{sc}}(\mathbf{r}_s)\left(1 - \frac{\theta}{2\pi}\right) + \int_C \left[\mathbf{E}^{\mathrm{sc}}(\mathbf{r}') \frac{\partial G_1(\mathbf{r}_s, \mathbf{r}')}{\partial \hat{n}} - G_1(\mathbf{r}_s, \mathbf{r}') \frac{\partial \mathbf{E}^{\mathrm{sc}}(\mathbf{r}')}{\partial \hat{n}}\right] dl' + \mathbf{E}^{\mathrm{inc}}(\mathbf{r}_s)\left(1 - \frac{\theta}{2\pi}\right) + \int_C \left[\mathbf{E}^{\mathrm{inc}}(\mathbf{r}') \frac{\partial G_1(\mathbf{r}_s, \mathbf{r}')}{\partial \hat{n}} - G_1(\mathbf{r}_s, \mathbf{r}') \frac{\partial \mathbf{E}^{\mathrm{inc}}(\mathbf{r}')}{\partial \hat{n}}\right] dl' \tag{5a}$$

$$0 = \mathbf{E}^{\mathrm{sc}}(\mathbf{r}_s)\left(\frac{\theta}{2\pi}\right) + \int_C \left[G_2(\mathbf{r}_s, \mathbf{r}') \frac{\partial \mathbf{E}^{\mathrm{sc}}(\mathbf{r}')}{\partial \hat{n}} - \mathbf{E}^{\mathrm{sc}}(\mathbf{r}') \frac{\partial G_2(\mathbf{r}_s, \mathbf{r}')}{\partial \hat{n}}\right] dl', \tag{5b}$$

where $\int$ is Cauchy's principal value of integration, $\mathbf{E}^{\mathrm{inc}}(\mathbf{r})$ and $\mathbf{E}^{\mathrm{sc}}(\mathbf{r})$ are the incident and scattered fields, respectively, $\mathbf{r}_s$ is a point on the DOE surface C, and $G_1(\mathbf{r}_s, \mathbf{r}')$ and $G_2(\mathbf{r}_s, \mathbf{r}')$ are the Green's functions for the regions 1 and 2. The phase θ is the angle subtended by the boundary at the point $\mathbf{r}_s = \mathbf{r}'$, which is a point in the contour integral at which a singularity occurs.[17] The total field $\mathbf{E}^{\mathrm{tot}}(\mathbf{r})$ is the sum of $\mathbf{E}^{\mathrm{inc}}(\mathbf{r})$ and $\mathbf{E}^{\mathrm{sc}}(\mathbf{r})$.

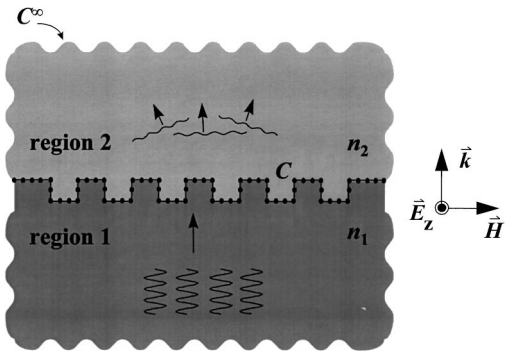

Fig. 5. Geometry of diffractive structure used in formulation of semi-infinite boundary element method.

To determine the total electric field with the BEM, one samples the contour C, which reduces Eqs. (5a) and (5b) to a single matrix equation in terms of the incident field values, E_n^{inc} and $Q_n^{\mathrm{inc}} = \partial E_n^{\mathrm{inc}}/\partial \hat{n}$, and the unknown scattered field values, E_n^{sc} and $Q_n^{\mathrm{sc}} = \partial E_n^{\mathrm{sc}}/\partial \hat{n}$, at the sample points. Solution of the matrix equation yields the scattered field values at the sampled nodes only; the field values elsewhere are determined by interpolation:

$$\mathbf{E}^{\mathrm{sc}}[\mathbf{r}'(\xi)] = \sum_{n=1}^{N} \hat{E}_n^{\mathrm{sc}}(\xi) = \sum_{n=1}^{N} [E_n^{\mathrm{sc}} \phi_1(\xi) + E_{n+1}^{\mathrm{sc}} \phi_2(\xi)], \tag{6a}$$

$$\mathbf{Q}^{\mathrm{sc}}[\mathbf{r}'(\xi)] = \sum_{n=1}^{N} \hat{Q}_n^{\mathrm{sc}}(\xi) = \sum_{n=1}^{N} [Q_n^{\mathrm{sc}} \phi_1(\xi) + Q_{n+1}^{\mathrm{sc}} \phi_2(\xi)]. \tag{6b}$$

In our analysis we used linear interpolation:

$$\phi_1(\xi) = (1 - \xi)/2, \tag{7a}$$

$$\phi_2(\xi) = (1 + \xi)/2, \tag{7b}$$

where $\xi = [-1, 1]$. The interpolated field values are used to determine the scattered field anywhere in space by

$$\mathbf{E}^{\mathrm{sc}}(\mathbf{r}) = \int_C \left[\mathbf{Q}^{\mathrm{sc}}(\mathbf{r}') G_2(\mathbf{r}, \mathbf{r}') - \mathbf{E}^{\mathrm{sc}}(\mathbf{r}') \frac{\partial G_2(\mathbf{r}, \mathbf{r}')}{\partial \hat{n}}\right] dl', \qquad \mathbf{r} \in 2, \tag{8}$$

and the total field is obtained by summing the scattered field with the incident field. Determination of the field anywhere in space allows one to quantify the performance of the DOE as indicated by step 4 in Fig. 1.

If the DOE has planar symmetry about the axis of propagation, the induced fields on the DOE are also symmetric. Thus one can formulate a symmetric BEM to reduce further the computational effort and memory requirements needed in analysis.[13] However, to take advantage of these reductions, the incident field must also have planar symmetry.

The resulting semi-infinite and symmetric formulation of the BEM (SSBEM) reduces the order of the system of equations by a factor of 4 and the memory requirements by a factor of 16, as compared with the traditional formulation. Nonetheless, to decrease further the computational time required for design, we implemented the SSBEM on a multiprocessor, or multi-CPU, parallel computer.[13] To illustrate the computational advantages afforded by a parallel approach, we applied the SSBEM to the analysis of an electrically large binary lens (300 λ in diameter) that required 712 Mbytes of memory. In comparison with the performance of a single CPU, the speed with which the structure was analyzed increased by 75% with each additional CPU. This resulted in a decrease in execution time from 12 h for a single CPU to 2.33 h with

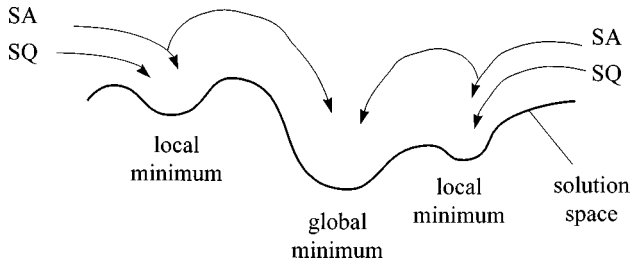

Fig. 6. Terrain of solutions navigated by SA and SQ optimization routines.

8 CPU's. In the subsection 2.C we discuss the optimization routines used in the synthesis algorithm, indicated as step 5 in Fig. 1.

C. Optimization Methods

In this section we discuss our implementation of the SA and SQ optimization routines, as illustrated in Fig. 6. In SA[18,19] the performance metric is first evaluated for a candidate profile to which subsequent changes are made. After each change the performance metric is reevaluated. If performance is enhanced, the change is accepted unconditionally. However, if performance is diminished, the change is accepted on the basis of Maxwell–Boltzmann statistics:

$$P(e, T) = \exp(-e/T), \tag{9}$$

where T is a parameter equivalent to the temperature of the system and e is the error. As the temperature decreases, the probability that a nonenhancing profile will be accepted decreases also. The critical factor in SA is the determination of a cooling schedule that allows the system to find its minimum state and, thereby, the globally optimum solution. If cooled too quickly, i.e., quenched, the system is likely to find a local minimum as opposed to the global one. For $T = 0$ (which we refer to as SQ), only enhancing profiles are accepted. As a result, the system obtains the local minimum that is closest to the initial state (see Fig. 6). However, because the system moves only in a direction that minimizes the error, it does so rapidly. For the design of electrically large diffractive elements that use vector-based diffraction models, this factor is critical. In Section 3 we present designs generated with both SA and SQ.

3. APPLICATIONS

In this section we apply our synthesis algorithm to the design of a subwavelength lens and a 1-to-2 focusing beam splitter. The objective of the first design is to maximize the diffraction efficiency of a subwavelength lens, whereas the objective for the 1-to-2 focusing beam splitter is to maximize diffraction efficiency into the $+1$ and -1 diffracted orders. The designs presented below were performed with 8 CPU's on a Silicon Graphics Power Challenge Array (R8000 CPU's) that had 2 Gbytes of main memory. Design specifications are presented below.

A. Subwavelength Lens Design

The first example of SWDOE design is a lens used to focus 10-μm infrared radiation onto a detector. The lens is designed to have a 100-μm focal length and a 96-μm diameter, which corresponds to an f-number of $f/1.04$. The lens was assumed to be fabricated in fused silica ($n = 1.5$) with a minimum feature of 1 μm and an etch depth of 10 μm. The lens must focus 70% of its incident radiation onto a 20-μm region on the detector. The continuous-phase lens that corresponds to these design requirements is represented in Fig. 7. Given the current state of technology, fabrication of this lens is unrealistic. Therefore we considered the design of a binary lens.

Application of Farn's extended technique to the continuous lens of Fig. 7 without consideration of fabrication constraints produced the binary lens represented in Fig. 8(a). The ability of the element to focus an incident plane wave is demonstrated clearly by the gray-scale image of the electric-field magnitude represented in Fig. 8(b). The intensity profile in the focal plane is represented in Fig. 8(c). The diffraction efficiency of the lens within the 20-μm window was calculated to be 76.45%.

Unfortunately, this lens cannot be fabricated. Application of the fabrication constraints, 1-μm minimum feature and 10-μm etch depth, yields the lens represented in Fig. 8(d). That the diffraction efficiency of this lens is reduced to only 50.29% is evident in Figs. 8(e) and 8(f). In fact, one can see in Fig. 8(e) that the focal spot has actually shifted away from the lens, an indication that the power of the lens has been weakened.

However, as shown in Figs. 8(g)–8(i), this loss in performance is recovered after approximately 135 iterations of simulated annealing. (The time per iteration was approximately 8 min and it converged in approximately 18 h.) In Figs. 8(h) and 8(i) one can see that the focus of the lens is now in the desired plane and that the energy within this plane is well contained within the desired 20-μm window. The final lens in Fig. 8(g) has a 72.54% diffraction efficiency, which is comparable to that of the lens in Fig. 8(a). However, we note that the lens in Fig. 8(h) satisfies our fabrication constraints whereas that of Fig. 8(a) does not.

Our confidence in the algorithm's ability to perform optimization was bolstered after careful comparison between the initial lens profile and the final profile. The initial subwavelength profile of Fig. 8(a) assumed a 20-μm etch depth, which corresponds to 2π phase. Quantization to a 10-μm etch depth reduced this phase to π, yet retained zone spacings appropriate for a 2π-phase lens. However, the final profile of Fig. 8(g) exhibits zone spacings that are consistent with a π-phase lens. Thus the algorithm found a solution that makes physical sense.

B. 1-to-2 Focusing Beam Splitter

Our second design example is a 1-to-2 focusing fan-out element. The incident illumination was assumed to be a

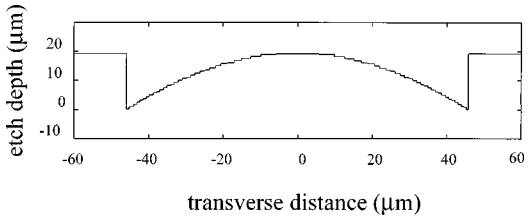

Fig. 7. Continuous-phase lens used in subwavelength design.

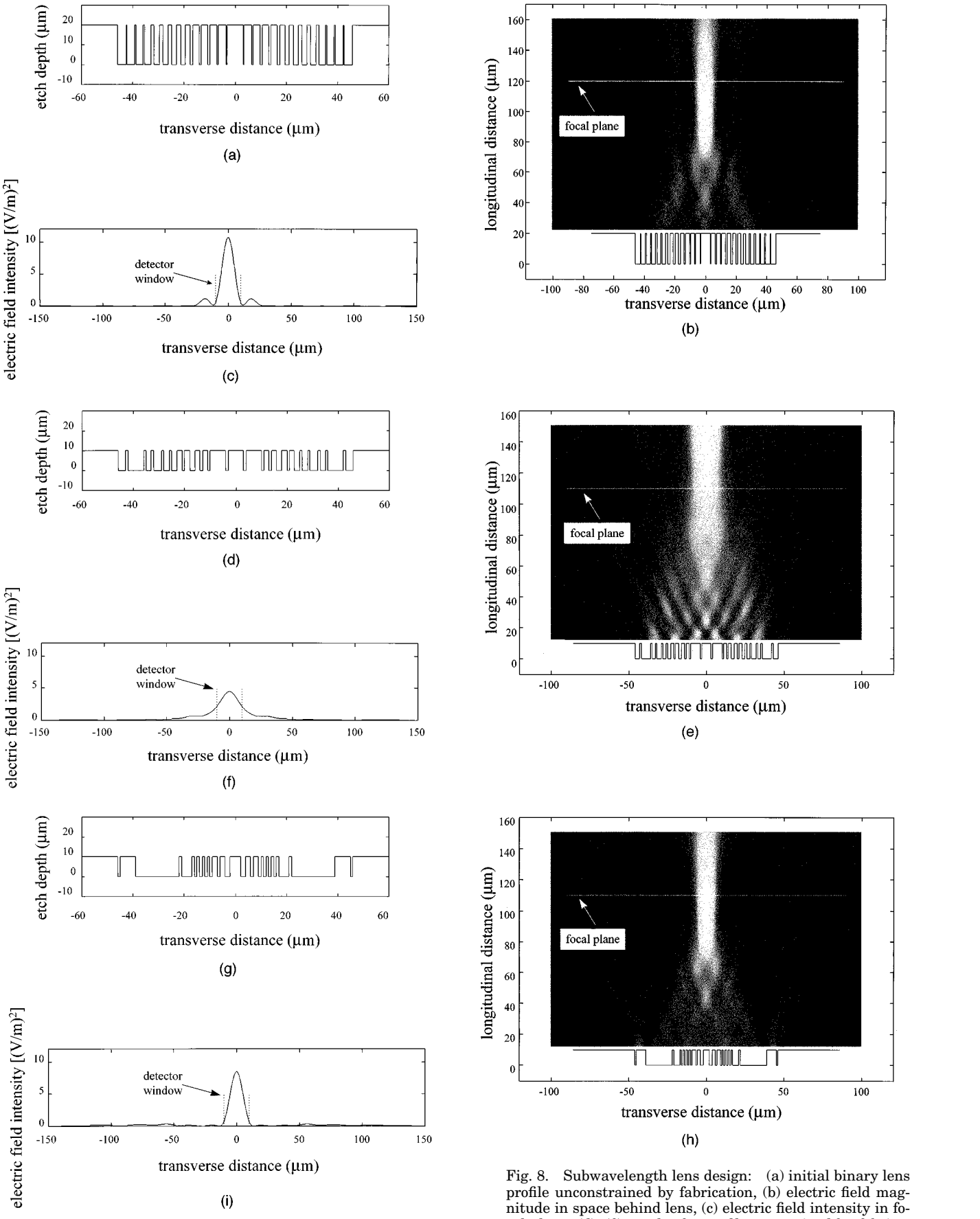

Fig. 8. Subwavelength lens design: (a) initial binary lens profile unconstrained by fabrication, (b) electric field magnitude in space behind lens, (c) electric field intensity in focal plane, (d)–(f) results for profile constrained by fabrication, and (g)–(i) results for final profile.

plane wave with a 1-μm wavelength. The output beams are separated by 139.5 μm at the detector plane 100 μm behind the element, which corresponds to an angular separation of 69.8°. We assumed that the element was fabricated in silicon with a 55.67-μm width. The minimum feature and etch depth were assumed to be 0.3 μm and 1 μm, respectively. The objective of the design was to maximize the diffraction efficiency within a 20-μm window centered about each spot.

To determine the initial input, we could have used a scalar-based Dammann grating; however, as the feature size is reduced in comparison with the wavelength, the Dammann grating no longer performs as a multiple beam splitter. Instead, the initial input was a simple 1×2 lenslet array created by placing two off-axis lenses, one with an off-axis angle of $+34.9°$ and the other with an angle of $-34.9°$, next to each other. Each lens has an f-number of $f/3.59$. The results of our design are summarized in Fig. 9. Figure 9(a) is the initial profile used as input to the algorithm. Figures 9(b) and 9(c) are representations of the electric field magnitude in the space behind the element and the intensity in the detector plane, respectively. For this design the diffraction efficiency into the two spots is only 39.20%.

The profile generated after six days of SQ iterations, represented in Fig. 9(d), produces 61.29% diffraction efficiency. Improvement in element performance is evident when one compares Figs. 9(e) and 9(f) with Figs. 9(b) and 9(c). Note especially in Fig. 9(e) that more of the diffracted light is concentrated into the individual foci than in Fig. 9(b). This example highlights the extent to which computational costs limit the practical design of subwavelength elements. Because of the electrically large nature of the element, each iteration took approximately 25 min.

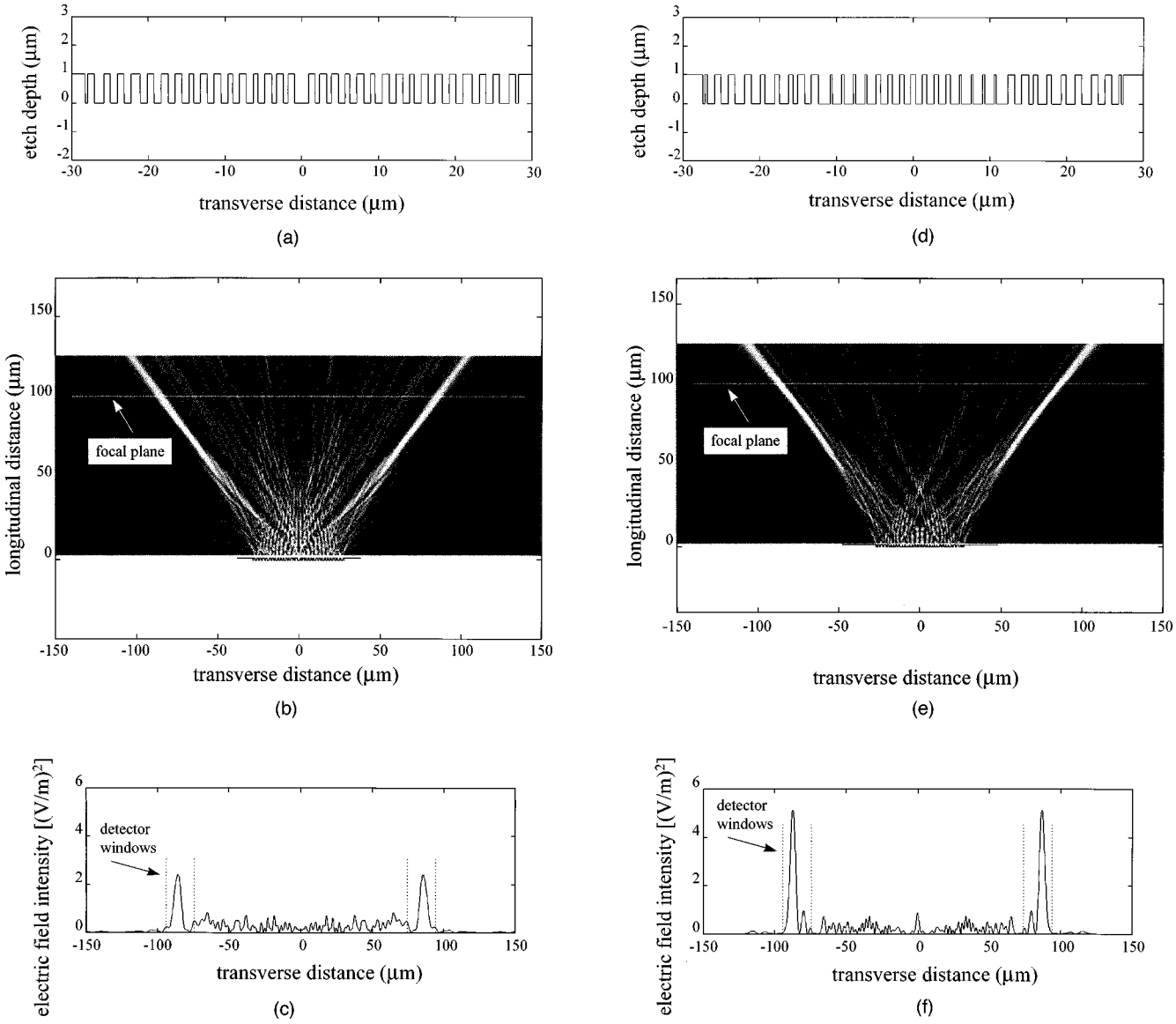

Fig. 9. Subwavelength design of 1-to-2 fan-out: (a) Initial profile, (b) electric-field magnitude in space behind fan-out, (c) electric field intensity in detector plane, and (d)–(f) results for final profile.

Our decision to use SQ as opposed to SA in the design was thus one of expedience. Had we used SA, execution of this design would have taken much longer.

4. CONCLUSION

In this paper we have demonstrated the ability to synthesize finite, aperiodic subwavelength DOE's. To achieve this we developed two essential tools: an efficient model of finite aperiodic vector-based diffraction and a design method for finite, aperiodic subwavelength DOE's.

A critical consideration in our work was the computational costs associated with the design of realistic elements. To this end we developed the SSBEM, which does not require a closed boundary and exploits symmetry to reduce the number of computations. Further, we implemented the SSBEM on a parallel computer.

We also extended Farn's technique for designing infinitely periodic SWDOE's to include finite, aperiodic SWDOE's. This technique was used to design binary DOE's whose performance emulated that of multilevel DOE's. These profiles were used as the initial DOE profiles in synthesis algorithms that use SSBEM to analyze diffraction.

Finally, we used our synthesis algorithms to design a subwavelength lens and a 1-to-2 focusing beam splitter. To the best of our knowledge, these designs represent the first documented account of the synthesis of finite, aperiodic SWDOE's.

APPENDIX A

The semi-infinite boundary integral equations are formulated by defining the solution space represented in Fig. 5, which consists of two unbounded, or semi-infinite, regions. Region 1 contains the DOE, and region 2 is free space. We apply the two-dimensional time-harmonic wave equation within each region. The inhomogeneous wave equation is used in region 1, where we assume the incident wave originates, and in region 2 we apply the homogeneous wave equation

$$0 = \nabla^2 u_2^{\text{tot}}(\rho) + \beta_2^2 u_2^{\text{tot}}(\rho), \qquad \rho \in 2, \tag{A1}$$

$$-f(\rho) = \nabla^2 u_1^{\text{tot}}(\rho) + \beta_1^2 u_1^{\text{tot}}(\rho), \qquad \rho \in 1, \tag{A2}$$

where $u^{\text{tot}} = \mathbf{E}_z^{\text{tot}}$ for TE polarization and $u^{\text{tot}} = \mathbf{H}_z^{\text{tot}}$ for TM. The wave numbers in region 1 and 2 are $\beta_i = 2\pi(\epsilon_{r,i})^{1/2}/\lambda_0$, $i = 1, 2$, and $f(\rho)$ represents the source term. The constants $\epsilon_{r,1}$ and $\epsilon_{r,2}$ are the permittivities of regions 1 and 2 relative to free space, i.e., $\epsilon_{r,i} = \epsilon_i/\epsilon_0$.

One casts Eqs. (A1) and (A2) into boundary integral equations by applying Green's second identity:

$$u_2^{\text{tot}}(\rho) = \int_C \left[G_2(\rho, \rho') u_2^{\text{tot}}(\rho') - u_2^{\text{tot}}(\rho') \frac{\partial G_2(\rho, \rho')}{\partial \hat{n}_2} \right] \mathrm{d}l', \qquad \rho \in 2, \tag{A3}$$

$$u_1^{\text{tot}}(\rho) = u_1^{\text{inc}}(\rho) + \int_C \left[G_1(\rho, \rho') u_1^{\text{tot}}(\rho') - u_1^{\text{tot}}(\rho') \frac{\partial G_1(\rho, \rho')}{\partial \hat{n}_1} \right] \mathrm{d}l', \qquad \rho \in 1, \tag{A4}$$

where $u^{\text{tot}}(\rho)$ and $v_i^{\text{tot}}(\rho') = \partial u_i^{\text{tot}}(\rho')/\partial \hat{n}_i$ represent the total field and its normal derivative and

$$u_1^{\text{inc}}(\rho) = \int_{C^\infty} f(\rho') G_1(\rho, \rho') \mathrm{d}l'. \tag{A5}$$

The vector from the origin to the observation point is $\rho(x, y)$, and the vector from the origin to the source point is $\rho'(x', y')$. The two-dimensional free-space Green's functions are

$$G_i(\rho, \rho') = \frac{1}{4j} H_o^{(2)}(\beta_i|\rho - \rho'|) = \frac{1}{4j} H_o^{(2)}\{\beta_i[(x - x')^2 + (y - y')^2]^{1/2}\}, \qquad i = 1, 2, \tag{A6}$$

where $H_o^{(2)}(\beta|\rho - \rho'|)$ is the zeroth-order Hankel function of the second kind.

Equations (A3) and (A4) represent a system of two equations in four unknowns, $u_i^{\text{tot}}(\rho')$ and $v_i^{\text{tot}}(\rho')$, $i = 1, 2$, which is indeterminate. One can solve it by applying boundary conditions at C:

$$u_1^{\text{tot}}(\rho') = u_2^{\text{tot}}(\rho') \equiv u^{\text{tot}}(\rho'), \qquad \rho' \in C \tag{A7}$$

$$\frac{1}{p_1} \frac{\partial u_1^{\text{tot}}(\rho')}{\partial \hat{n}_1} = -\frac{1}{p_2} \frac{\partial u_2^{\text{tot}}(\rho')}{\partial \hat{n}_2} \equiv u^{\text{tot}}(\rho'), \tag{A8}$$

where $p_i = 1$ for TE polarization and $p_i = \epsilon_i$ for TM. Equation (A7) represents the continuity of the tangential field component across the contour C and Eq. (A8) the normal derivative boundary condition. The minus sign in Eq. (A8) accounts for $\hat{n} = \hat{n}_1 = -\hat{n}_2$.

To avoid numerical errors that result when the boundary integral equations are applied to closed boundaries and the frequency of the illuminating radiation is a resonant frequency of the structure, we formulate the boundary integral equations in terms of the scattered fields:

$$u^{\text{tot}}(\rho) = u^{\text{inc}}(\rho) + u^{\text{sc}}(\rho). \tag{A9}$$

Substitution of Eq. (A9) into Eqs. (A3) and (A4) yields

$$0 = u^{\text{sc}}(\rho) + \int_C \left[u^{\text{sc}}(\rho') \frac{\partial G_2(\rho, \rho')}{\partial \hat{n}} - p_2 G_2(\rho, \rho') u^{\text{sc}}(\rho') \right] \mathrm{d}l' + u^{\text{inc}}(\rho) + \int_C \left[u^{\text{inc}}(\rho') \frac{\partial G_2(\rho, \rho')}{\partial \hat{n}} - p_2 G_2(\rho, \rho') u^{\text{inc}}(\rho') \right] \mathrm{d}l', \qquad \rho \in 2, \tag{A10}$$

$$0 = u^{\mathrm{sc}}(\rho) + \int_C \left[p_1 G_1(\rho, \rho') u^{\mathrm{sc}}(\rho') - u^{\mathrm{sc}}(\rho') \frac{\partial G_1(\rho, \rho')}{\partial \hat{n}} \right] \mathrm{d}l', \qquad \rho \in 1. \quad \text{(A11)}$$

To arrive at this we used the identity

$$\int_C \left[p_1 G_1(\rho, \rho') v^{\mathrm{inc}}(\rho') - u^{\mathrm{inc}}(\rho') \frac{\partial G_1(\rho, \rho')}{\partial \hat{n}} \right] \mathrm{d}l' = 0, \qquad \rho \in 1. \quad \text{(A12)}$$

One can solve Eqs. (A10) and (A11) by confining the observation vector to the boundary of the DOE, $\rho = \rho_s$. However, care must be exercised because of singularities that exist when $\rho_s = \rho'$. These singularities are evaluated by integrating around the singularity in the limit as ρ' approaches ρ_s with Cauchy's principal value of integration. The resulting boundary integral equations are

$$\begin{aligned} 0 = {} & u^{\mathrm{sc}}(\rho_s)\left(1 - \frac{\theta}{2\pi}\right) + \int_C \left[u^{\mathrm{sc}}(\rho') \frac{\partial G_2(\rho_s, \rho')}{\partial \hat{n}} - p_2 G_2(\rho_s, \rho') u^{\mathrm{sc}}(\rho') \right] \mathrm{d}l' + u^{\mathrm{inc}}(\rho_s)\left(1 - \frac{\theta}{2\pi}\right) \\ & + \int_C \left[u^{\mathrm{inc}}(\rho') \frac{\partial G_2(\rho_s, \rho')}{\partial \hat{n}} - p_2 G_2(\rho_s, \rho') u^{\mathrm{inc}}(\rho') \right] \mathrm{d}l', \end{aligned} \quad \text{(A13)}$$

$$0 = u^{\mathrm{sc}}(\rho_s)\left(\frac{\theta}{2\pi}\right) + \int_C \left[p_1 G_1(\rho_s, \rho') u^{\mathrm{sc}}(\rho') - u^{\mathrm{sc}}(\rho') \frac{\partial G_1^{\mathrm{tot}}(\rho_s, \rho')}{\partial \hat{n}} \right] \mathrm{d}l', \quad \text{(A14)}$$

where θ is the angle of the surface extending into region 1 at the singularity. Equations (A13) and (A14) are repeated in the body of the text as Eqs. (5a) and (5b). Once it is determined, the incident field can be added to the scattered electric field $u^{\mathrm{sc}}(\rho')$ on the boundary and used to calculate the total field anywhere in region 2:

$$u^{\mathrm{tot}}(\rho) = \int_C \left[u^{\mathrm{tot}}(\rho') \frac{\partial G_1(\rho, \rho')}{\partial \hat{n}} - p_1 G_1(\rho, \rho') u^{\mathrm{tot}}(\rho') \right] \mathrm{d}l', \qquad \rho \in 2. \quad \text{(A15)}$$

J. N. Mait can be reached by telephone at 301-394-2462, by fax at 301-394-5420, and by e-mail at mait@arl.mil.

REFERENCES

1. T. K. Gaylord and M. G. Moharam, "Analysis and applications of optical diffraction by gratings," Proc. IEEE **73**, 894–937 (1985).
2. M. W. Farn, "Binary gratings with increased efficiency," Appl. Opt. **31**, 4453–4458 (1992).
3. H. Haidner, J. T. Sheridan, J. Schwider, and N. Streibl, "Design of a blazed grating consisting of metallic subwavelength binary grooves," Opt. Commun. **98**, 5–10 (1993).
4. M. Schmitz, R. Brauer, and O. Bryngdahl, "Phase gratings with subwavelength structures," J. Opt. Soc. Am. A **12**, 2458–2462 (1995).
5. Z. Zhou and T. J. Drabik, "Optimized binary, phase-only, diffractive optical element with subwavelength features for 1.55 μm," J. Opt. Soc. Am. A **12**, 1104–1112 (1995).
6. E. Noponen, J. Turunen, and F. Wyrowski, "Synthesis of paraxial-domain diffractive elements by rigorous electromagnetic theory," J. Opt. Soc. Am. A **12**, 1128–1133 (1995).
7. D. W. Prather, M. S. Mirotznik, and J. N. Mait, "Design of subwavelength diffractive optical elements using a hybrid finite element-boundary element method," in *Diffractive and Holographic Optics Technology III*, I. Cindrich and S. H. Lee, eds., Proc. SPIE **2689**, 14–23 (1996).
8. D. W. Prather, M. S. Mirotznik, and J. N. Mait, "Boundary integral methods applied to the analysis of diffractive optical elements," J. Opt. Soc. Am. A **14**, 34–43 (1997).
9. D. H. Raguin, "Subwavelength structured surfaces: theory and applications," Ph.D. dissertation (University of Rochester, Rochester, N.Y., 1993).
10. J. N. Mait, "Understanding diffractive optic design in the scalar domain," J. Opt. Soc. Am. A **12**, 2145–2158 (1995).
11. M. Born and E. Wolf, *Principles of Optics* (Pergamon, Oxford, UK, 1980).
12. P. Lalanne and D. Lamercier-Lalanne, "On the effective medium theory of subwavelength periodic structures," J. Mod. Opt. **43**, 2063–2085 (1996).
13. D. W. Prather, "Analysis and synthesis of finite aperiodic diffractive optical elements using rigorous electromagnetic models," Ph.D. dissertation (University of Maryland, College Park, Md., 1997).
14. J. N. Mait, D. W. Prather, and M. S. Mirotznik, "Design and optimization of finite aperiodic subwavelength diffractive optical elements having arbitrary phase profiles," presented at the OSA 1996 Annual Meeting, Rochester, N.Y., Oct. 20–24, 1996.
15. D. W. Prather, M. S. Mirotznik, and J. N. Mait, "Boundary element method for vector modeling diffractive optical elements," in *Diffractive and Holographic Optics Technology II*, I. Cindrich and S. H. Lee, eds., Proc. SPIE **2404**, 28–39 (1995).
16. K. Hirayama, E. N. Glytsis, T. K. Gaylord, and D. W. Wilson, "Rigorous electromagnetic analysis of diffractive cylindrical lenses," J. Opt. Soc. Am. A **13**, 2219–2231 (1996).
17. S. Kagami and I. Fukai, "Application of boundary-element method to electromagnetic field problems," IEEE Trans. Microwave Theory Tech. **MTT-32**, 455–461 (1984).
18. S. Kirkpatrick, C. D. Gelatt, and M. P. Vecchi, "Optimization by simulated annealing," Science **220**, 671–680 (1983).
19. M. A. Seldowitz, J. P. Allebach, and D. W. Sweeney, "Synthesis of digital holograms by direct binary search," Appl. Opt. **26**, 2788–2798 (1987).